# Reaction of 5−40 eV Ions with Self-Assembled Monolayers†

**Xiangdong Qin, Tochko Tzvetkov, and Dennis C. Jacobs***

*Department of Chemistry and Biochemistry, University of Notre Dame, Notre Dame, Indiana 46556*

*Received: August 15, 2005; In Final Form: November 17, 2005*

The reaction of 5−40 eV $O^+$ and $Ne^+$ ions with alkanethiolate and semifluorinated alkanethiolate self-assembled monolayers (SAMs) is studied under ultrahigh vacuum (UHV) conditions. Whereas $Ne^+$ simply sputters fragments from the surface, $O^+$ can also abstract surface atoms and break C−C bonds in both the hydrocarbon and fluorocarbon SAM chains. Isotopic labeling experiments reveal that $O^+$ initially abstracts hydrogen atoms from the outermost two carbon atoms on an alkanethiolate SAM chain. However, the position of the isotopic label quickly becomes scrambled along the chain as the SAM is damaged through continuous ion bombardment. Scanning tunneling microscopy (STM) monitors changes in the SAM conformational structure at various stages during 5 eV ion bombardment. STM images indicate that $O^+$ reacts less efficiently with dodecanethiolate molecules packed internally within a structural domain than it does with molecules adsorbed at domain boundaries or near defect sites. STM images recorded after $Ne^+$ bombardment suggest that $Ne^+$ attacks the SAM exclusively near the domain boundaries. Taken collectively, these experiments advance our understanding of the degradation pathways suffered by polymeric satellite materials in the low-earth orbit (LEO) space environment.

## 1. Introduction

The interaction of hyperthermal energy (1−500 eV) particles with surfaces can activate a variety of chemical processes at the gas/surface interface, including abstraction, elimination, insertion, implantation, and oxidation.[1,2] An interesting feature of the hyperthermal energy region is that it provides the system with sufficient energy to activate the barrier to virtually any chemical reaction, even those which do not occur under thermal conditions. On the other hand, the collision energy is often low enough to avoid severe surface damage from sputtering. From a chemical perspective, hyperthermal is the most interesting and promising energy region to study.

Spacecraft materials placed in the low-earth orbit (LEO) environment are subjected to an extremely harsh chemical and physical attack which can readily induce severe erosion and failure of the materials.[3] Degradation/erosion in space is primarily caused by the bombardment of hyperthermal particles. In addition to the neutral constituents in LEO (100−350 km) such as O, $N_2$, $O_2$, He, and Ar, a weak plasma consisting mostly of $O^+$, $NO^+$, $O_2^+$, and electrons is present at a density of $10^5$−$10^6$ per $cm^3$.[4] The most abundant neutral and ionic species are O and $O^+$, respectively. At an altitude of 300 km, the relatively large orbital velocity (∼7 km/s) of a spacecraft gives rise to a 5 eV collision between an ambient oxygen atom and the exterior surface of the spacecraft. Polymers are an attractive spacecraft material due to their desirable properties such as moldability, flexibility, low density, electrical properties, and low cost.[5] Great effort has been taken to measure erosion rates and to elucidate degradation mechanisms for polymeric materials in both space- and ground-based experiments. The mission of the Long Duration Exposure Facility (LDEF) satellite and the launching of a series of Materials International Space Station Experiments (MISSE) were designed to measure the erosion yields of a wide variety of polymers in space. Theoretical simulations of the interaction of hyperthermal atoms with materials have been attempted with increasing success.[2,6−9] At the same time, a number of experimental groups have attempted to simulate the LEO environment in the laboratory. Most of these experiments were designed to study the interaction of neutral 5 eV oxygen atoms with polymeric materials, since atomic oxygen is the most abundant species in LEO.[10−14] However, laboratory-based simulations of the LEO environment utilizing a neutral O atom source have often failed to achieve as high of an etching rate as that measured in space.[15] Potential synergistic effects involving electron, photon, and ion bombardment may accelerate the reactivity of O atoms in LEO.[16] To date, the operative mechanisms responsible for the erosion of spacecraft surfaces and the dependence of these mechanisms on the interaction conditions (e.g., incident flux, collision energy, incident angle, surface temperature, and synergistic effects) remain largely unknown. A detailed understanding of operative erosion mechanisms will provide invaluable information for designing next generation spacecraft materials.

Self-assembled monolayers (SAMs) are ordered, functionalized molecular assemblies that form spontaneously by adsorption of an active surfactant with a specific affinity of its headgroup to an appropriate substrate.[17] An alkanethiolate SAM on Au(111) is the most studied SAM system due to its ease of preparation and the stability of the SAM in an atmospheric environment.[18−20] Self-assembled organic films are attractive, because one can tune their properties by changing only part of the chain without modifying the entire chain. For example, by changing the end group of an alkanethiol ($HS(CH_2)_nCH_3$) from $-CH_3$ to $-OH$, the properties of the film will switch from hydrophobic to hydrophilic. For studying the interaction of ions with organic films, a SAM is advantageous over bulk polymers, because it will not charge up and it presents a highly characterized and reproducible surface at the vacuum interface. Both experimental and theoretical investigations have explored the interaction of

† Part of the special issue "William Hase Festschrift".

* To whom correspondence should be addressed. E-mail: jacobs.2@nd.edu.

10.1021/jp054596u CCC: $33.50 
Published on Web 12/17/2005

hyperthermal atoms and ions with alkanethiolate SAMs and functionalized SAMs.[21−37]

Particle/surface collisions at hyperthermal energies can result in the abstraction of an atom or a group of atoms from the surface, leaving the surface with an active radical site. The nascent radical site can react with species generated from subsequent ion bombardment, or it can cross-link with another radical site. Unfortunately, the detailed reaction mechanisms for these chemical modifications are largely unclear. To determine the role that $O^+$ plays in materials degradation within LEO, hyperthermal $O^+$ is targeted at alkanethiolate and semifluorinated alkanethiolate SAMs that serve as models for polyethylene and Teflon, respectively. Both the structure and the chemical composition of the SAM are closely monitored as a function of ion dose and energy. Characterizing the erosion mechanisms for SAMs exposed to $O^+$ is paramount to better understanding the degradation of polymeric materials used in space applications and to designing improved materials that are resistant to attack in LEO.

## 2. Experimental Section

The experiments are conducted in an ultrahigh vacuum (UHV) chamber described elsewhere.[38,39] Briefly, the apparatus consists of three differentially pumped chambers: the source and buffer chambers contain the ion transport optics, the main scattering chamber houses the surface sample and diagnostic tools, and the rotatable detector chamber contains a quadrupole mass spectrometer. The main chamber pressure stays below $1 \times 10^{-9}$ Torr during the ion scattering experiments. Disks of single-crystal Au(111) (10 mm diameter × 2 mm thick) are produced from Monocrystal Company with a miscut of less than 0.5°. The cleaning procedure for a Au(111) crystal involves repeated cycles of 500 eV $Ar^+$ sputtering at acute angles followed by surface annealing at 550 °C. The cleanliness of the surface is monitored by X-ray photoelectron spectroscopy (XPS), and the surface structure is verified by low-energy electron diffraction (LEED). The clean monocrystal is then removed from the UHV chamber and quickly submerged into a freshly prepared 1 mM alkanethiol/ethanolic solution for 24 h to form the SAM. After the sample is removed from the solution, it is thoroughly rinsed in absolute ethanol and dried under blown nitrogen. Quickly, the substrate is relocated into the UHV chamber and left under vacuum for 18−24 h at room temperature to remove any excess solvent. Decanethiol or dodecanethiol are used to form a self-assembled monolayer, because they exhibit long-term stability in air and vacuum. Increasing the alkane chain length beyond 12 carbons would reduce the layer's electrical conductivity, promote charging of the surface, and detrimentally alter the incident and outgoing ion trajectories.

Three isotopically labeled dodecanethiols (C-10, C-11, and C-12) are employed in which all of the hydrogen atoms bound to the 10th, 11th, or 12th carbon atom, respectively, of 1-dodecanethiol are selectively substituted with deuterium atoms.[40] Dodecanethiol (Aldrich) and 1H,1H,2H,2H-perfluorodecanethiol (Oakwood Chemicals) are used as received without further purification.

A monoenergetic beam of mass-selected $O^+$, prepared by flowing CO(g) through a plasma electron impact ion source, is directed at the SAM, 45° to the surface. The scattered ionic products are analyzed with mass, energy, and angle resolution. Due to the low incident ion flux and poor detection sensitivity for neutral species, this study is limited to analyzing ionic products. All experiments are performed at $T = 300$ K with the ~10 nA ion beam irradiating the sample. For the ex situ scanning tunneling microscopy (STM) studies, a 5 eV $O^+$ or $Ne^+$ beam is directed at normal incidence to the surface. After exposure, the sample is removed from the UHV chamber and imaged with a Molecular Imaging PicoPlus SPM. All STM images are collected under atmospheric conditions at sample biases of ±0.5−0.7 V and tunneling currents of 4−12 pA. The molecularly resolved surface structures appeared stable through repetitive scans over a period of hours.

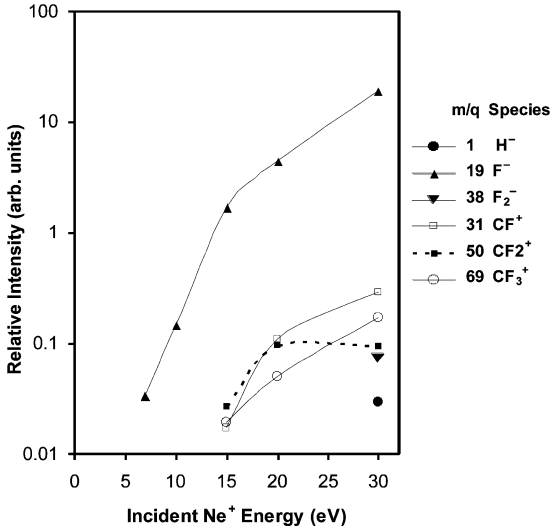


**Figure 1.** Yields of scattered ionic products from $Ne^+$ + perfluorodecanethiolate SAM.

## 3. Results

**3.1. Reaction Products.** The chemical modifications and erosion of SAMs under hyperthermal energy ion bombardment can be significant. One strategy for deciphering the complex chemistry in these systems is to detect in situ the scattered ionic products as a function of the collision energy, the identity of the projectile ion, and the chemical functionality of the SAM. Synthetic methods can be employed to alter the molecular chains comprising the SAM.

*3.1.1. $Ne^+$ + Semifluorinated SAM.* A semifluorinated SAM derived from 1H,1H,2H,2H-perfluorodecanthiol ($CF_3(CF_2)_7(CH_2)_2SH$) absorbed on Au(111) is chosen as a well-characterized model for a fluoropolymer. The semifluorinated SAM is exposed to 5−30 eV $Ne^+$, while the scattered product ions are mass-resolved and collected. Figure 1 shows the intensities of the scattered ionic products as a function of incident energy. The most abundant product ion, $F^-$ ($m/q = 19$), increases rapidly with incident ion energy. No additional negative ions are detected until the incident energy reaches 30 eV, where both $H^-$ ($m/q = 1$) and $F_2^-$ ($m/q = 38$) appear with weak intensity. For the positive ion products, the threshold energy to detect $CF^+$ ($m/q = 31$), $CF_2^+$ ($m/q = 50$), and $CF_3^+$ ($m/q = 69$) is approximately 15 eV. The yields of the scattered ionic products generally increase with the incident $Ne^+$ energy.

*3.1.2. $O^+$ + Semifluorinated SAM.* Many more ionic products are detected when the semifluorinated SAM is bombarded with a hyperthermal $O^+$ beam than with a $Ne^+$ beam. Figure 2 shows how the yields of the scattered ionic products depend on incident energy for 5−30 eV $O^+$ incident on the SAM. At all collision energies under study, charge inversion of the incident ion produces a significant amount of $O^-$ ($m/q = 16$). Exhibiting a very similar energy dependence to that seen for incident $Ne^+$, the $F^-$ ($m/q = 19$) product displays a threshold near 7 eV followed by a sharp rise with incident $O^+$ energy. The appearance threshold for both abstraction products, $OF^-$ ($m/q$

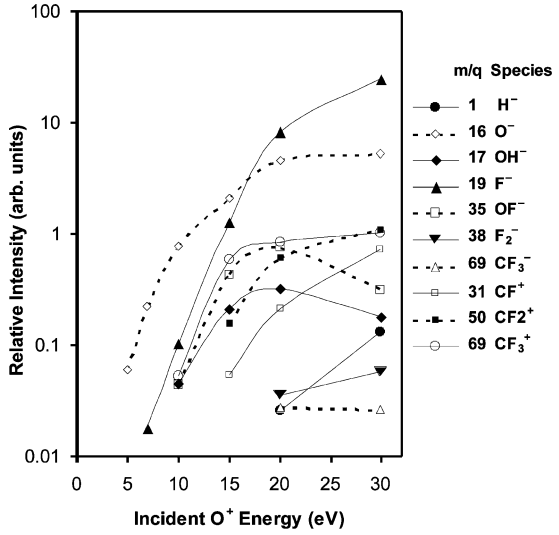


**Figure 2.** Yields of scattered ionic products from $O^+$ + perfluorodecanethiolate SAM.

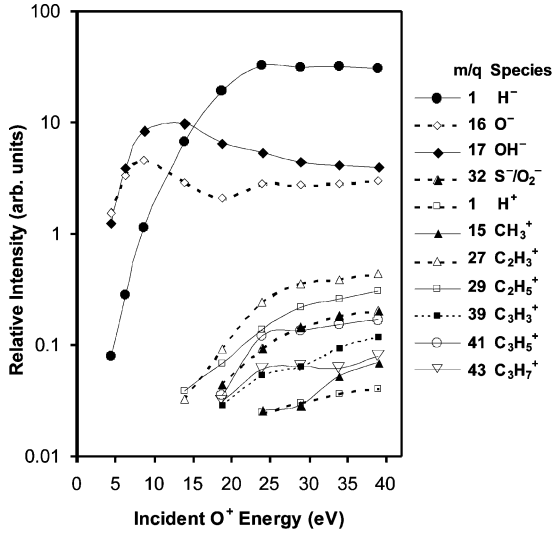


**Figure 3.** Yields of scattered ionic products from $O^+$ + decanethiolate SAM.

= 37) and $OH^-$ ($m/q$ = 17), is near 10 eV. At far less intensity, $H^-$ ($m/q$ = 1), $F_2^-$ ($m/q$ = 38), and $CF_3^-$ ($m/q$ = 69) are detected only when the incident energy exceeds 20 eV. The $CF_3^+$ ($m/q$ = 69) product appears at 10 eV but begins to fragment into $CF^+$ ($m/q$ = 31) and $CF_2^+$ ($m/q$ = 50) when the incident energy exceeds 15 eV.

*3.1.3. $O^+$ + Alkanethiolate SAM.* The reaction behavior is more complex when $O^+$ ions bombard a decanethiolate SAM at energies between 5 and 40 eV. Figure 3 shows a plot of the yields for all scattered positive and negative ions versus the incident energy. Negative ions generally scatter in greater abundance than do positive ions, and they appear at lower incident energies. At 5 eV, the abstraction product, $OH^-$ ($m/q$ = 17), is produced with comparable intensity as the charge inversion product, $O^-$ ($m/q$ = 16); hydride ejection, $H^-$ ($m/q$ = 1), occurs with much lower probability. At energies beyond 15 eV, hydride ions represent the dominant ionic product for this system. The yield of $S^-/O_2^-$ ($m/q$ = 32) increases monotonically after its appearance energy (20 eV). With the exception of a trace amount of $H^+$ ($m/q$ = 1), all of the scattered positive ions can be traced to the ejection and decay of alkyl cations. To determine whether the signal at $m/q$ = 29 corresponds to $C_2H_5^+$ or $HCO^+$, mass spectra of the scattered ions

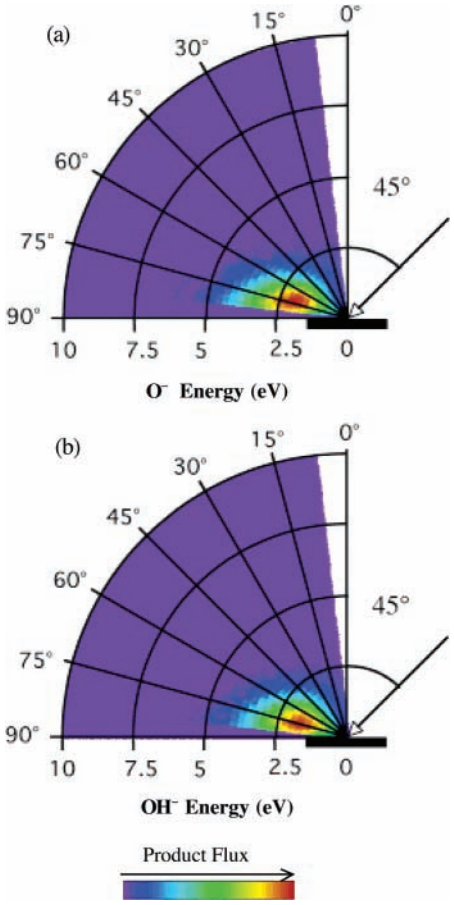


**Figure 4.** Angle- and energy-resolved distributions for (a) $O^-$ and (b) $OH^-$ products. 8.7 eV $O^+$ ions approached the surface at a 45° incident angle, as the arrow indicates in the figure. The radial coordinate indicates the exit energy of the detected products. The exit angle is marked with respect to the surface normal. The flux of the scattered ions, presented in a false color scale, is plotted against the exit angle and energy. Each plot is individually scaled such that the maximum intensity is plotted in red.

are compared when $^{16}O^+$ versus $^{18}O^+$ is targeted at the SAM. Because the signal at $m/q$ = 31 does not arise above the background noise level when $^{16}O^+$ is replaced by $^{18}O^+$, no more than 15% of the mass-29 signal can be attributed to $HCO^+$. The C2 species, $C_2H_3^+$ ($m/q$ = 27) and $C_2H_5^+$ ($m/q$ = 29), are produced in greater quantities than the C3 species, $C_3H_3^+$ ($m/q$ = 39), $C_3H_5^+$ ($m/q$ = 41), and $C_3H_7^+$ ($m/q$ = 43). These, in turn, are more abundant than $CH_3^+$ ($m/q$ = 15) or $H^+$ ($m/q$ = 1), regardless of the incident energy.

*3.1.3.1. Hydrogen Abstraction.* Figure 3 shows that $OH^-$ is the only reaction product emerging from the $O^+$ + decanethiolate SAM system that contains the incident ion below 20 eV incident energy. Figure 4 shows the remarkable similarity between the angle-resolved energy distribution of the scattered $O^-$ and $OH^-$ species. Of particular interest is the precise site on the hydrocarbon chain from which the oxygen ion abstracts a hydrogen atom. Isotopic labeling of the hydrocarbon chain by synthetic methods allows one to record the site dependence to abstraction. Qin et al. reported that incident $O^+$ initially abstracts hydrogen from essentially the top two carbon atoms on the alkyl chain.[40] Here, we report how the fluence of incident ions affects the site specificity to the reaction.

The integrated intensities, $I_{OD}$ and $I_{OH}$, are calculated by integrating the $OD^-$ and $OH^-$ signal intensities, respectively, over all outgoing energies. $P_{OD}$, defined in eq 1, is the percentage of all abstracted H/D that originates from the labeled

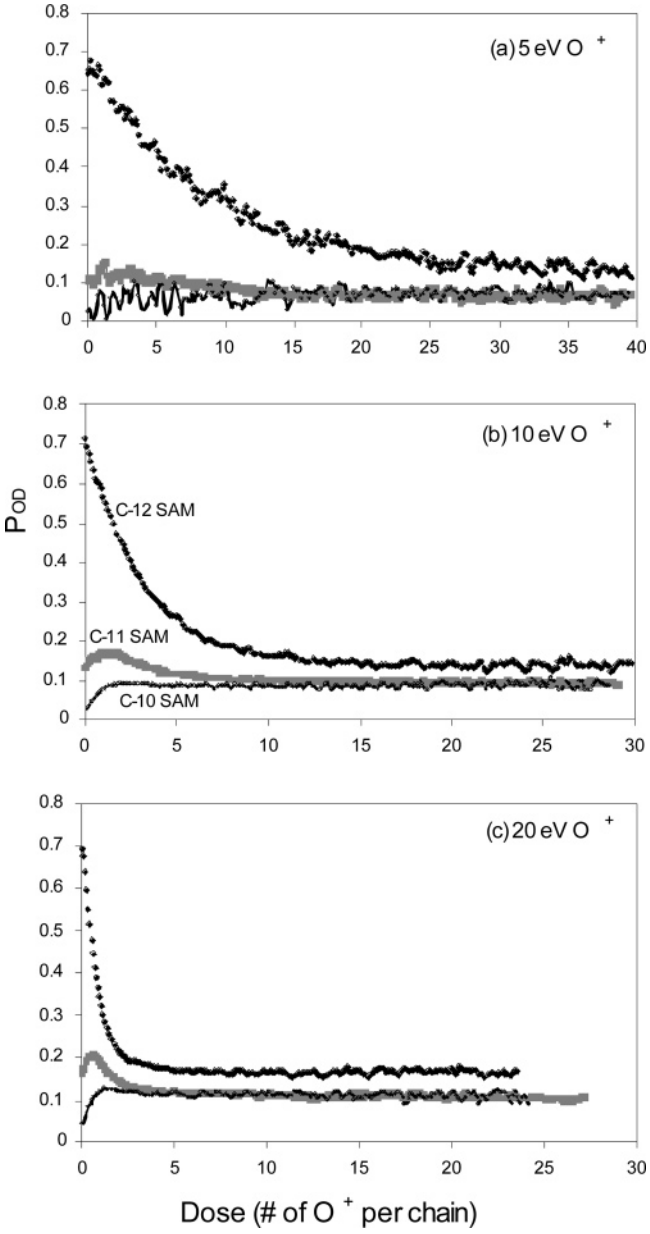


**Figure 5.** Dependence of $P_{OD}$ on $O^+$ dose at an incident energy of (a) 5 eV, (b) 10 eV, and (c) 20 eV.

position in the SAM.

$$P_{OD} = \frac{I_{OD}}{I_{OH} + I_{OD}} \times 100\% \quad (1)$$

Parts a, b, and c of Figure 5 show the dependence of $P_{OD}$ on the dose of incident ions at incident energies of 5, 10, and 20 eV, respectively. As the SAM becomes damaged/eroded by continuous ion bombardment, $P_{OD}$ evolves accordingly. For the C-12 SAM, $P_{OD}$ always undergoes a rapid single-exponential decay with $O^+$ dose, while C-11 and C-10 SAMs show an initial rise in $P_{OD}$ followed by a slower decay.

**3.2. Structural Damage.** STM provides a real-space, molecularly resolved image of the SAM structure that reveals the packing, periodicity, morphology, and defects. Figure 6 shows a molecularly resolved STM image of a dodecanethiolate SAM on Au(111). The image contains several large gold terraces separated by gold steps. On each terrace, the surface comprises a mosaic of conformational domains with a lattice structure of

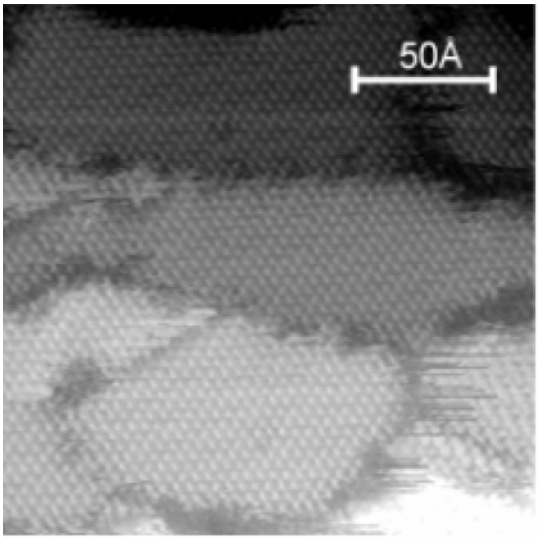


**Figure 6.** STM image of an unirradiated dodecanethiolate SAM on Au(111).

$(\sqrt{3} \times \sqrt{3})R30°$. The conformational domains are separated by molecular-scale domain boundaries.

The domain boundary network is decorated by pitlike defects that do not exist on a clean Au(111) surface. The measured pit depth is 2.5 Å, consistent with a Au(111) single-atom step height. This suggests that the pits are vacancies in the Au layer rather than in the alkanethiol layer.[41] Researchers have speculated that these pits are formed by the ejection of excess Au atoms from the surface when the Au(111) herringbone reconstructs as thiol molecules adsorb on the surface.[42,43] On a densely packed SAM, the vacancy islands are covered with alkanethiolate molecules.

*3.2.1. $O^+$ + Alkanethiolate SAM.* Figure 7 shows two STM images of dodecanethiolate SAMs after $O^+$ bombardment. Figure 7a is recorded after a dose of one 5 eV $O^+$ ion per five alkanethiolate chains. Within this image, most of the sizable domain areas remain largely intact. Some small depressions can be seen at various points within the intact domains. The most significant ion-induced alteration to the SAM is that the domain boundaries have broadened significantly upon $O^+$ exposure. Figure 7b shows the SAM after a dose that is 2.5 times greater than that in Figure 7a. Clearly, at higher dose, the domain boundaries broaden further, and the ordered domain size decreases.

*3.2.2. $Ne^+$ + Alkanethiolate SAM.* To learn the relative contribution of ion-induced structural damage that is caused by physical rather than chemical means, STM images of a SAM exposed to one 5 eV $Ne^+$ per two alkanethiolate chains is recorded and displayed in Figure 8. Two observations are noted. First, unlike the $O^+$ + alkanethiolate SAM system, there are no indentations within the large intact domains. Second, the broadening of the domain boundaries is not as prominent as it was for the case of $O^+$ + alkanethiolate SAM. Consequently, a larger fraction of the image is occupied by intact domains, when $Ne^+$ rather than $O^+$ is the projectile.

## 4. Discussion

**4.1. Comparison of $O^+$ versus $Ne^+$ on Semifluorinated SAMs.** Spacecraft in LEO often utilize fluoropolymers as a thermal coating material to protect the vehicle from overheating when exposed to direct solar irradiation.[44] To provide insight into how oxygen ions may potentially contribute to the degradation of fluoropolymers in LEO, a semifluorinated SAM

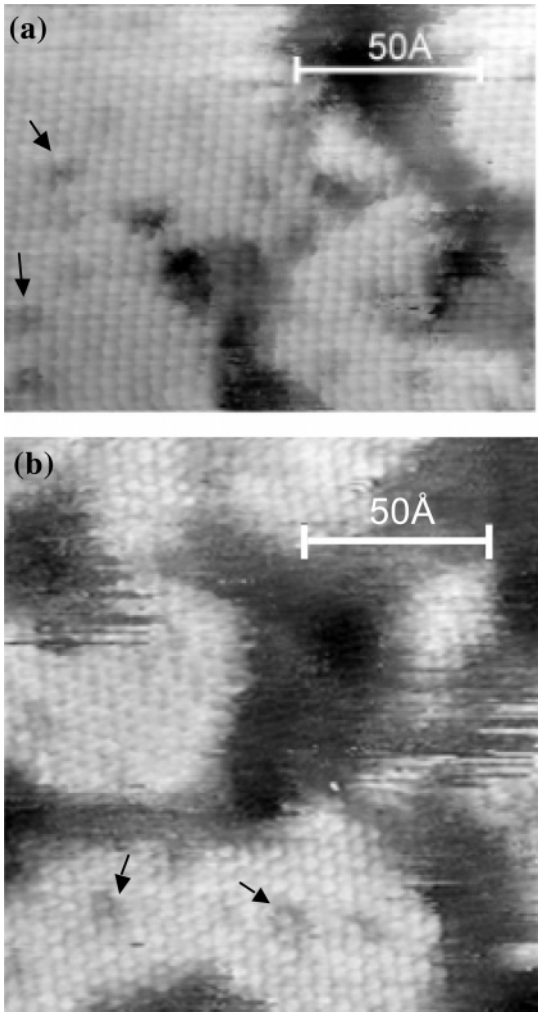


**Figure 7.** STM images of irradiated dodecanethiolate SAM on Au(111). The 5 eV $O^+$ dose is (a) 0.2 $O^+$/chain and (b) 0.5 $O^+$/chain. Examples of the observed indentations are indicated with arrows.

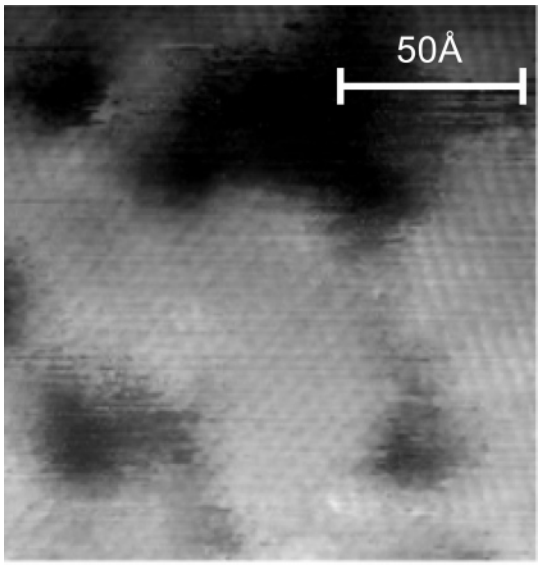


**Figure 8.** STM image of $Ne^+$-bombarded dodecanethiolate SAM on Au(111). The 5 eV $Ne^+$ dose is 0.5 $Ne^+$/chain.

is exposed to hyperthermal $O^+$, and the scattered products are detected. To further delineate the role of chemical and physical interactions in the overall erosion process, scattering experiments are compared using $Ne^+$ versus $O^+$ projectiles across the 5−30 eV energy range.

The yields of all scattered ionic products resulting from hyperthermal $Ne^+$ and $O^+$ ions striking a semifluorinated SAM are plotted in Figures 1 and 2, respectively. $Ne^+$ and $O^+$ show similar behavior in the production of positive ions ($CF^+$, $CF_2^+$, and $CF_3^+$). $O^+$ produces a wide range of anionic products ($H^-$, $F^-$, $F_2^-$, $O^-$, $OH^-$, $OF^-$, and $CF_3^-$), some containing the projectile itself. In contrast, $Ne^+$ yields only three anionic products ($H^-$, $F^-$, and $F_2^-$). Because anionic products frequently emerge from reactions involving the neutralized projectile, the more diverse set of anionic products resulting from $O^+$ bombardment can be attributed primarily to the higher reactivity of O relative to that of Ne. For example, the data demonstrate that O is capable of abstracting H and F from the semifluorinated SAM.

The formation of $CF^+$, $CF_2^+$, and $CF_3^+$ indicates that both incident ions can break the C−C bond when the incident energy exceeds 10 eV. The threshold energy to detect $CF_3^+$ is near 10 eV for $O^+$ and near 15 eV for $Ne^+$. Presumably, $O^+$ demonstrates a lower threshold than $Ne^+$, because $O^+$ can stabilize the transition state leading to C−C bond cleavage. The detection of fragments from the fluorocarbon chain is consistent with observations made for $O^+$ incident on a decanethiolate SAM (Figure 3), where alkyl cations appear at a similar incident energy. The higher yields of scattered fluorocarbon cations when $O^+$ rather than $Ne^+$ impacts the surface suggests that a fluorinated SAM will be damaged more readily by $O^+$ than by $Ne^+$.

Starting at 7 eV, both $Ne^+$ and $O^+$ can sputter $F^-$ from the semifluorinated SAM. The sputtering yield of $F^-$ increases rapidly with incident ion energy for both projectiles. The formation of $F^-$ shows no dependence on the identity of the incident ion, a result that suggests a pure physical sputtering mechanism. $F_2^-$ is also formed when either $O^+$ or $Ne^+$ collides with the surface. The formation of $F_2^-$ probably arises through a sputtering−abstraction mechanism, whereby a sputtered fluoride ion abstracts a second F atom as it leaves the surface.[45]

$O^+$ is more reactive than $Ne^+$, as evidenced by the fact that it can abstract atoms from the surface to produce $OH^-$ and $OF^-$. The abstraction of F is not surprising given the large concentration of fluorine atoms at the end of the chain. However, the formation of $OH^-$ is unexpected, since hydrogen atoms are only available beginning eight carbon atoms down the chain, and the isotopic labeling experiment (section 3.1.3.1) concluded that only hydrogen atoms bound to the top two carbon atoms on a dodcanethiolate SAM can be abstracted by oxygen. There is likely to be greater sensitivity to hydrogen than to fluorine, because $OH^-$ is formed by a stripping mechanism where the momentum of the projectile is barely altered by abstraction; consequently, the $OH^-$ product emerges with a larger velocity and survival probability.[40] In contrast, the $OF^-$ product emerges at lower velocities and suffers greater electron loss. Notwithstanding, the source of hydrogen in the SAM is perplexing. Contamination from intercalated, noncovalently bound thiol is unlikely, because the layers are stored under vacuum for 18−24 h before the scattering experiment begins. One alternative explanation for the small amount of $OH^-$ produced from the semifluorinated surface is that hydrogen abstraction occurs exclusively along the domain boundaries where entire chains are exposed. Alternatively, an incident $O^+$ ion may channel between neighboring fluorocarbon chains without losing much of its kinetic energy, reach the bottom of the chain, abstract a hydrogen atom, and return to the vacuum while retaining enough kinetic energy to be detected. This degree of extended penetra-

tion was also noted in the reaction of hyperthermal $O(^3P)$ with a semifluorinated SAM.[28]

Detection of $H^-$ from the semifluorinated SAM suggests that the hydride species are ejected from the exposed chains along a domain boundary or defect. The comparable energy dependence to the $H^-$ yield, irrespective of whether $O^+$ or $Ne^+$ is the projectile, indicates that the mechanism for $H^-$ ejection does not rely heavily on the chemical nature of the projectile but arises from physical sputtering.

**4.2. Comparison of $O^+$ on Alkanethiolate versus Semifluorinated SAMs.** The emergence of negatively charged ions outnumbers the production of positively charged ions when hyperthermal $O^+$ impacts either a semifluorinated or an alkanethiolate SAM, as seen in Figures 2 and 3. On an alkanethiolate SAM, the negative ions arise from inelastic scattering ($O^-$), abstraction ($OH^-$), and sputtering ($H^-$). Similarly, $O^-$, $OF^-$, and $F^-$ are formed when a semifluorinated SAM is exposed to $O^+$. Compared with $OH^-$ formed on the alkanethiolate SAM, $OF^-$ is produced with less yield and at a higher threshold energy due to the larger mass of the F atom. When the impinging energy is above 20 eV, some of the sputtered $F^-$ ions are able to abstract a F atom from a nearby chain to form the diatomic product, $F_2^-$. The special distributions of the scattered $F_2^-$ products rule out significant contribution to the signal of a product formed by two F atoms from the same hydrocarbon chain.

The mechanism for $H^-$ emergence from the alkanethiolate SAM is elucidated by comparing the $H^-$ signal for 20 eV $O^+$ versus 20 eV $Ne^+$ projectiles. Both experiments yielded $H^-$, indicating the existence of a pathway for forming $H^-$ that does not require oxygen. However, the $O^+$ projectile yielded 4 times as much $H^-$ as did the $Ne^+$ projectile. The enhancement in the $H^-$ signal when $O^+$ is employed could indicate that a portion of the $H^-$ signal arises from hydride elimination of a nascent product such as $H_2CO^-$,[46] that neutralization of $O^+$ generates a different electronically excited state in the SAM than does neutralization of $Ne^+$, and/or the oxygen projectile facilitates more facile electron attachment to H than does the neon projectile.

On an alkanethiolate SAM, $S^-/O_2^-$ ($m/q = 32$) appears when the incident energy is above 20 eV. When the isotopic variant, $^{18}O^+$, is first delivered to a fresh SAM, only $S^-$ ($m/q = 32$) is detected. With increased $^{18}O^+$ exposure, however, the $O_2^-$ ($m/q = 36$) signal develops quickly. Since the yield plots are collected at higher doses, the measured signal at $m/q = 32$ contains contributions from both $S^-$ and $O_2^-$. The formation of $S^-$ indicates that, at this energy, the incident $O^+$ is able to reach the headgroup of the SAM and break the Au−S bond, which can cause a whole alkanethiolate chain to desorb from the surface.[28] $O_2^-$ is formed when an incident $O^+$ picks up an O that is already trapped or incorporated in the SAM. The accumulation of oxygen in the irradiated SAM was independently verified by XPS.[39] It is difficult to ascertain the specific bonding configuration of oxygen incorporated into the SAM. Because the scattering experiments reported here were performed at low fluence, the absence of an ionic scattered product containing both C and O should not be interpreted as evidence that a C−O−C structure is not formed within the oxidized layer at high fluence. Furthermore, only scattered reaction products that depart at high velocity will have a finite probability for emerging with a negative charge.

As seen in Figure 3, alkyl cations are ejected when $O^+$ impacts the alkanethiolate SAM at higher energies. The appearance of a distribution of C2 species ($C_2H_3^+$ and $C_2H_5^+$) and C3 species ($C_3H_3^+$, $C_3H_5^+$, and $C_3H_7^+$) suggests that the C−C bond is broken by dissociative charge transfer, similar to the interaction of $O^+$ with isolated alkane molecules.[47] $C_2H_3^+$ comes from $H_2$ elimination of $C_2H_5^+$ in the gas phase. Similarly, $C_3H_3^+$ and $C_3H_5^+$ originate from $C_3H_7^+$. In contrast, only C1 species ($CF^+$, $CF_2^+$, and $CF_3^+$) are detected when $O^+$ collides with a semifluorinated SAM. Presumably, the larger mass of fluorine restricts the size of alkyl ions that can be ejected from the SAM.

The yields of both the positive and negative ions strongly correlate with the incident energy. Since $O^+$ is more likely to damage the SAM at higher incident energies, the scattered signals measured at higher incident energies may be artificially offset relative to the yields measured at lower energies. Nevertheless, the relative order of species in the yield plots is unlikely to be affected.

**4.3. Hydrogen Abstraction—Effect of $O^+$ Energy and Fluence.** Figure 4 shows the angle- and energy-resolved scattering distributions for $O^-$ and $OH^-$ products when 8.7 eV $O^+$ ions strike the surface at 45° incidence. Both products show strong forward scattering, indicating that the formation of $O^-$ and $OH^-$ involves a limited number of collisions with the surface. If the projectiles were to encounter multiple collisions with various SAM chains, the scattering distributions would exhibit little or no memory of the incident momentum vector. Furthermore, the angular distributions of $O^-$ and $OH^-$ are remarkably similar. The formation of $OH^-$ is consistent with a stripping mechanism whereby the oxygen projectile picks up a light hydrogen atom without altering its momentum significantly.

To determine the site from which the abstracted hydrogen atom originates, SAMs were prepared using isotopically labeled thiols. Previous studies demonstrated that $O^+$ initially abstracts H from only the top two carbon positions in the alkyl chain.[40] This pronounced site preference was also confirmed in theoretical simulations by Schatz and co-workers.[6,46] Figure 5 shows the dependence of $P_{OD}$ on the flux of $O^+$ incident at energies ranging from 5 to 20 eV. Although the data here have not been corrected for the influence of charge transfer, the trends of the curves are unlikely to be affected. The values of $P_{OD}$ for the three labeled SAMs depend dramatically on the dose of the incident ions. Since the deuterium labels are located on the top layers of the SAM, the $OD^-$ signal is expected to disappear as the SAM is eroded away with increasing $O^+$ exposure. Instead, $P_{OD}$ never vanishes but reaches an asymptotic value that depends on the labeled position; in the high-dose limit, $P_{OD}$ for the C-12 SAM is ∼50% greater than $P_{OD}$ for the C-10 and C-11 SAMs. After the film is damaged, the deuterium content appears to be proportional to the number of D atoms originally on the chain (the $-CD_3$ group on the C-12 SAM contains 50% more deuterium than the $-CD_2^-$ group on the C-10 and C-11 SAMs). This suggests that after a SAM chain is attacked by $O^+$, the positions of the D and H atoms remaining on the chain are efficiently scrambled.

There are several possible models that could explain how the scrambling occurs. When $O^+$ first strikes a SAM molecule, a likely outcome is that the projectile will abstract or sputter a hydrogen atom from the terminal methyl group, thus generating a methyl radical. A hydrogen atom will then migrate from the adjacent methylene position to the methyl position to form a more stable methylene radical. However, this unidirectional movement will only move hydrogen from the bottom of the chain to the top, and the model will not predict the experimental result at high dose. As an alternative model, a pseudorandom hydrogen hopping mechanism could lead to complete scram-

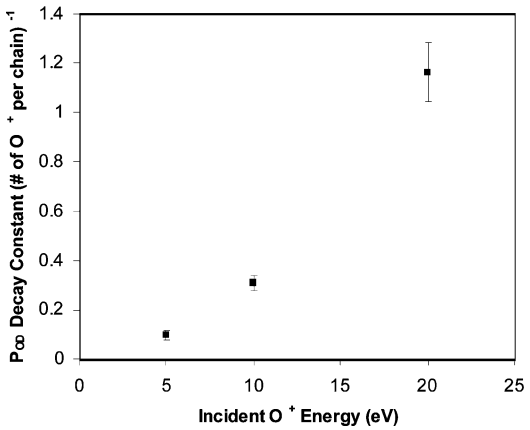


**Figure 9.** Dependence of the $P_{OD}$ decay constant on the $O^+$ incident energy.

bling. Once a H(D) is abstracted and a radical site is formed near the top of the chain, the H(D) next to the radical site can move to the radical site. If this step repeats itself without any site preference, the H(D) atoms can eventually move up and down their entire chain. If H(D) migration is fast enough, the H(D) atoms will become randomly distributed before a second incident $O^+$ strikes the same chain. On the basis of the ion beam current density used in the experiment, we have estimated that the average time between two sequential $O^+$ collisions with a single chain is approximately 20 min, allowing ample time for scrambling. This pseudorandom hydrogen hopping mechanism provides a means to sequester the D atoms and preserve the isotopic ratio while the chain is being eroded away. In addition to intrachain hydrogen hopping where the radical site migrates along a single chain, interchain hydrogen hopping can happen if the radical site migrates between chains. If interchain hydrogen hopping does occur, it must be limited to a few neighboring chains, or else a single radical site generated anywhere on a terrace could catalyze the rapid scrambling of all deuterium atoms on the terrace. The consequence of the latter scenario would be that the measured $P_{OD}$ will reach its asymptotic value much quicker than is observed experimentally. However, another plausible scrambling model is that $O^+$ can impulsively drive a deuterium atom from the end of the chain to deep within the film, where the displaced deuterium atom could be trapped inside the chain or be exchanged with a hydrogen atom from deeper inside the SAM.

The initial rate at which $P_{OD}$ changes with dose is highly energy dependent. For the C-12 SAM, $P_{OD}$ reaches an asymptote at a dose of less than five 20 eV $O^+$ ions per alkanethiolate chain. Approximately 15 10 eV $O^+$ ions are required to strike an alkanethiolate chain before $P_{OD}$ becomes constant. At 5 eV, more than 40 $O^+$ ions must collide with each chain before complete scrambling is achieved. The decay of $P_{OD}$ for a C-12 SAM reflects how rapidly SAM chains become damaged and consequently their H(D) atoms become scrambled. For the C-12 SAM, the decay curves can be fit with a single-exponential function, for which the decay constants are plotted in Figure 9. It is difficult to accurately extrapolate a damage threshold for $O^+$/SAM bombardment, but the data suggest that when $O^+$ is incident at an energy above 2 eV, extensive damage will occur to the SAM. At higher incident energies, the C−C bond within an alkanethiolate chain can be broken, facilitating a rapid decay in the value of $P_{OD}$ during the early stages of ion irradiation.

**4.4. Structural Damage Induced by 5 eV $O^+$ and $Ne^+$.** The distribution of scattered ions generated when 5 eV $O^+$ impacts an alkanethiolate SAM confirms the loss of hydrogen. In addition, XPS shows continuous carbon loss and oxidation of the alkane chain with increasing $O^+$ exposure.[39] The isotopic labeling experiment presented in the previous section reveals facile scrambling of the hydrogen and deuterium atom positions with only modest $O^+$ dose. The ensuing effects that these ion-induced chemical modifications have on the structure of the SAM are studied using ex situ STM. The SAM samples are removed from UHV following ion bombardment, and an STM image of the damaged SAM is recorded under atmospheric conditions. Although reactions in air can modify the chemical composition of the SAM, ex situ STM images of the bombarded SAMs are stable over time and often show highly ordered domains.

Figures 6−8 show STM images of an unexposed alkanethiolate SAM surface, a SAM exposed to 5 eV $O^+$, and a SAM exposed to 5 eV $Ne^+$. A closer look at Figure 7a reveals a series of newly formed indentations within the ordered domains. The indentations are uniform in size and are stable over a period of hours; therefore, they must represent chemical rather than conformational modifications. On the basis of the size of the image area and the $O^+$ dose, approximately one indentation (marked with an arrow in Figure 7) forms for every seven oxygen ions incident on a terrace. If each indentation within the STM image represents a missing carbon atom, then the etch rate on an intact domain is 3 times lower than that for a degraded SAM as measured by XPS. Figure 7b shows the result for a dose 2.5 times greater than that in Figure 7a. Although the number of indentations per unit surface area does not increase with the $O^+$ dose (part a versus part b of Figure 7), many of the nascent indentations are likely to be enveloped within the expanding domain boundaries, obscuring them in the STM image. At the higher dose, the domain boundaries are significantly broader, and the portion of the image occupied by ordered domains decreases from 78 to 60% between parts a and b of Figure 7. In contrast, the STM image of a SAM exposed to one 5 eV $Ne^+$ per two alkanethiolate chains is shown in Figure 8. The damage observed for the SAM bombarded by 5 eV $Ne^+$ is less extensive. Not only do the intact domains show no indentations when $Ne^+$ is the projectile, but just 10% of the SAM image (as opposed to 40% with $O^+$) is marked with disordered domain boundaries. Because $Ne^+$ does not produce any indentations on the intact domains despite ejecting $H^-$ ions, it is inferred that each of the indentations appearing in Figure 7 represents the loss of a carbon atom from the chain.

It is informative to compare the damage appearing within the STM images to that measured by XPS. As concluded in the previous XPS study,[39] an average of 0.38 C atoms are removed when one $O^+$ strikes one alkanethiolate chain. Because the XPS data were collected at a dose up to 50 times greater than that for the STM study, it is reasonable to assign the 0.38 C/$O^+$ reaction probability only to the damaged domain boundaries and not to the intact domains that are resistant to attack. Applying the XPS erosion rate to 22% of the area in Figure 7a that is occupied by damaged domain boundaries or Au vacancies, one predicts that 7.7 C atoms are lost per 100 × 100 Å$^2$ unit area. Accounting for the additional carbon loss (10.3 C atoms per 100 × 100 Å$^2$ unit area) from the indentations on the intact domains, the total erosion is 18 C atoms per 100 × 100 Å$^2$ at a dose of 0.2 $O^+$ per chain. Similarly, 35 C atoms per 100 × 100 Å$^2$ are lost from the damaged regions (40%) shown in Figure 7b, and 7.9 C atoms are lost from the intact domains. These losses combine to yield a total erosion of 43 C atoms per 100 × 100 Å$^2$ at a dose of 0.5 $O^+$ per chain. Consequently, the average erosion yield at either dose is 0.19

C per incident $O^+$. As the SAM becomes completely damaged at high $O^+$ dose, the erosion yield is predicted to converge on the value (0.38 C per incident $O^+$) determined by XPS.

## 5. Summary

Hyperthermal energy ions can inflict significant damage on a SAM through impulsive energy transfer, charge-transfer-induced electronic excitations, and a variety of chemical reactions. A complement of experiments has documented many of the degradation pathways by which a SAM is eroded and structurally modified. Mass spectrometry identifies the scattered ionic products when a hyperthermal $O^+/Ne^+$ impacts an alkanethiolate or semifluorinated alkanethiolate SAM. In addition to physical sputtering, $O^+$ can directly abstract hydrogen or fluorine atoms from predominantly the topmost layer of the SAM. Removal of an atom from a hydrocarbon SAM chain will initiate facile hydrogen migration along the chain and create opportunities for cross-linking between chains. In addition, an $O^+$ ion can remove carbon from the chain or incorporate oxygen into the SAM with significant probability (38% and 18%, respectively, for a 5 eV $O^+$ ion).[39] The site dependence to ion erosion not only demonstrates a strong propensity for abstraction to occur near the vacuum interface but is manifest in the preferential attack of molecules adsorbed at domain boundaries or near defect sites in contrast to those packed internally within a structural domain.

Comparatively, $Ne^+$ is less destructive than $O^+$ when the ions are targeted at a SAM. Fewer scattered products emerge from a $Ne^+$-bombarded SAM, and the resulting layer is less disordered than a SAM exposed to an equivalent amount of $O^+$. These results underscore the important influence of chemical effects as $O^+$ stabilizes reaction intermediates and lowers activation barriers far better than its $Ne^+$ counterpart.

This study sheds light on some of the complex mechanisms operative when hyperthermal energy ions bombard organic thin films. In particular, the results help increase our understanding of how polymeric materials degrade in the harsh low-earth orbit environment where the external surfaces of a spacecraft are bathed relentlessly in atomic oxygen, $O^+$ ions, electrons, and photons.

**Acknowledgment.** We thank Dr. Dong-Chan Lee and Prof. Luping Yu (U. of Chicago) for providing the isotopically labeled thiols and Prof. Diego Troya (Virginia Tech.), Dr. Lipeng Sun (Northwestern U.), and Prof. George Schatz (Northwestern U.) for helpful discussions around their simulations of the data. This work was conducted through the Center for Materials Chemistry in the Space Environment, a Multidisciplinary University Research Initiative supported by the Air Force Office of Scientific Research (F49620-01-1-0335).

## References and Notes

(1) Jacobs, D. C. *Annu. Rev. Phys. Chem.* **2002**, *53*, 379.
(2) Troya, D.; Schatz, G. C. *Int. Rev. Phys. Chem.* **2004**, *23*, 341.
(3) Leger, L. J.; Visentine, J. T. *J. Spacecr. Rockets* **1986**, *23*, 505.
(4) Murad, E. *Annu. Rev. Phys. Chem.* **1998**, *49*, 73.
(5) de Groh, K. K.; Banks, B. A.; Hammerstrom, A. M.; Youngstrom, E. E.; Kaminski, C.; Gummow, J. D.; Wright, D. "MISSE PEACE Polymers: An International Space Station Environmental Exposure Experiment,", NASA/TM-2001-211311.
(6) Troya, D.; Schatz, G. C. *J. Chem. Phys.* **2004**, *120*, 7696.
(7) Yan, T. Y.; Hase, W. L. *J. Phys. Chem. B* **2002**, *106*, 8029.
(8) Yan, T. Y.; Doubleday: C.; Hase, W. L. *J. Phys. Chem. A* **2004**, *108*, 9863.
(9) Yan, T. Y.; Hase, W. L.; Doubleday: C. *J. Chem. Phys.* **2004**, *120*, 9253.
(10) Zhang, J. M.; Garton, D. J.; Minton, T. K. *J. Chem. Phys.* **2002**, *117*, 6239.
(11) Zhang, J. M.; Minton, T. K. *High Perform. Polym.* **2001**, *13*, S467.
(12) Iskanderova, Z. A.; Kleiman, J. I.; Gudimenko, Y.; Tennyson, R. C. *J. Spacecr. Rockets* **1995**, *32*, 878.
(13) Yokota, K.; Tagawa, M.; Ohmae, N. *J. Spacecr. Rockets* **2003**, *40*, 143.
(14) Golub, M. A.; Wydeven, T. *Polym. Degrad. Stab.* **1988**, *22*, 325.
(15) Koontz, S. L.; Albyn, K.; Leger, L. J. *J. Spacecr. Rockets* **1991**, *28*, 315.
(16) Kleiman, J. I.; Iskanderova, Z. A.; Perez, F. J.; Tennyson, R. C. *Surf. Coat. Technol.* **1995**, *76*−*77*, 827.
(17) Ulman, A. *An introduction to ultrathin organic film: from Langmuir*−*Blodgett to self-assembly*; Academic Press: Boston, MA, 1991.
(18) Ulman, A. *Chem. Rev.* **1996**, *96*, 1533.
(19) Schreiber, F. *Prog. Surf. Sci.* **2000**, *65*, 151.
(20) Poirier, G. E. *Chem. Rev.* **1997**, *97*, 1117.
(21) Li, G.; Bosio, S. B. M.; Hase, W. L. *J. Mol. Struct.* **2000**, *556*, 43.
(22) Isa, N.; Gibson, K. D.; Yan, T.; Hase, W.; Sibener, S. J. *J. Chem. Phys.* **2004**, *120*, 2417.
(23) Yan, T. Y.; Isa, N.; Gibson, K. D.; Sibener, S. J.; Hase, W. L. *J. Phys. Chem. A* **2003**, *107*, 10600.
(24) Yan, T. Y.; Hase, W. L. *J. Phys. Chem. A* **2001**, *105*, 2617.
(25) Yan, T. Y.; Hase, W. L. *Phys. Chem. Chem. Phys.* **2000**, *2*, 901.
(26) Day, B. S.; Morris, J. R. *J. Phys. Chem. B* **2003**, *107*, 7120.
(27) Day, B. S.; Shuler, S. F.; Ducre, A.; Morris, J. R. *J. Chem. Phys.* **2003**, *119*, 8084.
(28) Wagner, A. J.; Wolfe, G. M.; Fairbrother, D. H. *J. Chem. Phys.* **2004**, *120*, 3799.
(29) Torres, J.; Perry, C. C.; Bransfield, S. J.; Fairbrother, D. H. *J. Phys. Chem. B* **2002**, *106*, 6265.
(30) Gibson, K. D.; Isa, N.; Sibener, S. J. *J. Chem. Phys.* **2003**, *119*, 13083.
(31) Wade, N.; Evans, C.; Jo, S. C.; Cooks, R. G. *J. Mass Spectrosc.* **2002**, *37*, 591.
(32) Wade, N.; Evans, C.; Pepi, F.; Cooks, R. G. *J. Phys. Chem. B* **2000**, *104*, 11230.
(33) Somogyi, A.; Smith, D. L.; Wysocki, V. H.; Colorado, R.; Lee, T. R. *J. Am. Soc. Mass Spectrom.* **2002**, *13*, 1151.
(34) Smith, D. L.; Selvan, R.; Wysocki, V. H. *Langmuir* **2003**, *19*, 7302.
(35) Shukla, A. K.; Futrell, J. H. *Int. J. Mass Spectrom.* **2003**, *228*, 563.
(36) Shukla, A. K.; Futrell, J. H.; Sen, A. D. *J. Chem. Phys.* **2003**, *118*, 11217.
(37) Burroughs, J. A.; Hanley, L. *Anal. Chem.* **1994**, *66*, 3644.
(38) Quinteros, C. L.; Tzvetkov, T.; Jacobs, D. C. *J. Chem. Phys.* **2000**, *113*, 5119.
(39) Qin, X.; Tzvetkov, T.; Jacobs, D. C. *Nucl. Instrum. Methods Phys. Res., Sect. B* **2003**, *203*, 130.
(40) Qin, X. D.; Tzvetkov, T.; Liu, X.; Lee, D. C.; Yu, L. P.; Jacobs, D. C. *J. Am. Chem. Soc.* **2004**, *126*, 13232.
(41) Edinger, K.; Golzhauser, A.; Demota, K.; Woll, C.; Grunze, M. *Langmuir* **1993**, *9*, 4.
(42) Poirier, G. E. *Langmuir* **1997**, *13*, 2019.
(43) Yang, G. H.; Liu, G. Y. *J. Phys. Chem. B* **2003**, *107*, 8746.
(44) Rasoul, F. A.; Hill, D. J. T.; George, G. A.; Odonnell, J. H. *Polym. Adv. Technol.* **1996**, *9*, 24.
(45) Quinteros, C. L.; Tzvetkov, T.; Qin, X.; Jacobs, D. C. *Nucl. Instrum. Methods Phys. Res., Sect. B* **2001**, *182*, 187.
(46) Sun, L.; Schatz, G. C. *J. Phys. Chem. B* **2005**, *109*, 8431.
(47) Levandier, D. J.; Chiu, Y. H.; Dressler, R. A. *J. Chem. Phys.* **2004**, *120*, 6999.